Vortex lattices in the superconducting phases of doped topological insulators and heterostructures

Hsiang-Hsuan Hung, Pouyan Ghaemi, Taylor L. Hughes, and Matthew J. Gilbert

Vortex Lattices in the Superconducting Phases of Doped Topological Insulators and Heterostructures

Hsiang-Hsuan Hung,[1, 2] Pouyan Ghaemi,[3] Taylor L. Hughes,[3] and Matthew J. Gilbert[1, 2]

[1]*Department of Electrical and Computer Engineering, University of Illinois, Urbana, Illinois 61801*
[2]*Micro and Nanotechnology Laboratory, University of Illinois, 208 N. Wright St, Urbana IL 61801*
[3]*Department of Physics, University of Illinois, Urbana, Illinois 61801*

Majorana fermions are predicted to play a crucial role in condensed matter realizations of topological quantum computation. These heretofore undiscovered quasiparticles have been predicted to exist at the cores of vortex excitations in topological superconductors and in heterostructures of superconductors and materials with strong spin-orbit coupling. In this work we examine topological insulators with bulk *s*-wave superconductivity in the presence of a vortex-lattice generated by a perpendicular magnetic field. Using self-consistent Bogoliubov-de Gennes, calculations we confirm that beyond the semi-classical, weak-pairing limit that the Majorana vortex states appear as the chemical potential is tuned from either side of the band edge so long as the density of states is sufficient for superconductivity to form. Further, we demonstrate that the previously predicted vortex phase transition survives beyond the semi-classical limit. At chemical potential values smaller than the critical chemical potential, the vortex lattice modes hybridize within the top and bottom surfaces giving rise to a dispersive low-energy mid-gap band. As the chemical potential is increased, the Majorana states become more localized within a single surface but spread into the bulk toward the opposite surface. Eventually, when the chemical potential is sufficiently high in the bulk bands, the Majorana modes can tunnel between surfaces and eventually a critical point is reached at which modes on opposite surfaces can freely tunnel and annihilate leading to the topological phase transition previously studied in the work of Hosur *et al.*[1].

I.   INTRODUCTION

Majorana fermions, quasi-particle excitations which are their own antiparticle, were originally proposed in high-energy physics but[2] have now arrived at the forefront of condensed matter physics. It is predicted that the braiding of multiple Majorana modes will cause non-trivial rotations within the degenerate many-body Hilbert space and forms the backbone of many proposed topological quantum computing architectures[3–9]. Within condensed matter physics, there exist many candidate systems which are predicted to harbor Majorana fermions. One of the earliest of such candidates is the fractional quantum Hall effect at filling factor $\nu = \frac{5}{2}$[10] the physics of which may be described by the Moore-Read pfaffian wavefunction[11]. While this state is yet to be experimentally confirmed, tantalizing evidence observed in tunneling in quantum constrictions points to the fact that the $\nu = \frac{5}{2}$ fractional quantum Hall state does possess non-Abelian statistics as would be necessitated by the presence of Majorana fermions[12]. Beyond the fractional quantum Hall states, other possible systems thought to contain Majorana fermions are the $p_x + ip_y$ superconductors[3,8,11,13,14] where the relevant Majorana modes are predicted to appear as bound-states on exotic half-quantum vortices, which were recently observed in magnetic force microscopy experiments performed in Sr_2RuO_4[15]. In addition to fractional quantum Hall states and superconductors, there has been an abundance of proposals to realize Majorana fermions in materials with strong-spin orbit coupling. Notable examples are proximity induced superconductivity in 3D topological insulators (TIs)[16], bulk superconductivity in doped TIs[1] and semiconductors coupled proximity coupled to s-wave superconductors[17–20]. Indeed, the latter proposals have led to exciting measurements in high mobility quantum wire - *s*-wave superconductor systems[21].

In this article we will focus on the two mechanisms proposed in TI materials. As is now well-known, TIs are materials which possess an insulating bulk but contain robust metallic states that are localized on their surfaces[22–32]. We will consider time-reversal invariant 3D topological insulators which harbor an odd number of massless Dirac cones on each surface. As mentioned, there currently exist two proposals that utilize topological insulators as a platform for the observation of Majorana fermions. The first of which is to consider an *s*-wave superconductor/topological insulator heterostructure in which a superconductor is coupled to the topological insulator via the proximity effect and subjected to a vortex-producing magnetic field.[16] In Fu and Kane's pioneering work,[16] they show that in the *s*-wave superconductor/TI heterostructure, the interface between the TI and the superconductor behaves similar to a spinless chiral *p*-wave superconductor yet without breaking time reversal symmetry. As such, Majorana fermions will reside in the vortex cores[16,33] so long as the quantized magnetic flux lines penetrating the system are broad[34].

On the other hand, another strategy to realize Majorana fermions is to consider vortex bound-states in a 3D TI with bulk *s*-wave superconductivity[1,6,35]. Bulk superconductivity in doped topological insulators has been

observed in recent experiments that dope Bi_2Se_3 with copper.[36–38] For this particular material the nature of the order parameter is still under debate, but the two most probable options are s-wave, or an inter-orbital topological pairing parameter[39]. There is an opportunity to observe Majorana fermions in both cases, but for the purpose of this work we will only consider the s-wave case. Recent work[1] reveals that, while doped topological insulators that develop s-wave pairing may harbor Majorana bound states in the vortices, the Majorana fermions do not survive for all doping levels. Specifically, there exists a critical chemical potential, μ_c, at which point the system undergoes a topological (vortex) phase transition. This phase transition can be regarded as a topology change in the 1D electronic structure of vortex lines from a system which supports gapless end states to one that does not. Therefore, only at chemical potentials below the critical value, the doped superconducting Bi_2Se_3 supports Majorana modes at the vortex ends (places where vortex lines intersect the surface). The work of Ref. 1 provided a semiclassical treatment in the infinitesimal pairing limit, but such an approach might be inadequate to capture important quantum effects. One such effect that cannot be determined this way is the zero-point energy contribution of the vortex core states which could shift the states away from the zero energy gapless point and invalidate the previous analysis. In the weak-pairing limit the physics is determined by the structure exactly at the Fermi-surface, and it is possible that the energy spectrum away from the Fermi-level can serve to renormalize the location of the critical point. If the critical point is sufficiently shifted toward the band-edge, it could be that there is never a viable doping-range over which the Majorana fermions can be observed. Calculations provided in this article go beyond the semi-classical, and infinitesimal weak-pairing limit are thus essential to confirm the previous results.

In both TI based approaches we have thus far discussed, there is an additional assumption underlying the resultant physical predictions, namely that the vortices are completely isolated. However, this may not be the most appropriate or experimentally relevant picture for the observation of Majorana states in either type of TI approach. Thus, in this article, we examine the behavior of 3D topological insulators with bulk s-wave superconductivity in the vortex lattice limit as a function of doping level. The paper is organized in the following fashion: In Sections II, and III, we introduce the 3D topological insulator model Hamiltonian which is used for each of the subsequent calculations, and the background for the self-consistent calculations respectively. In Section IV, we present the results of our calculations for three separate geometries (a)periodic boundary conditions with vortex rings (b) open boundary conditions with vortex lines terminating on the TI surface (c) an inhomogeneously doped heterostructure with open boundary conditions. We find that as the chemical potential is moved from the gap into the bulk bands, the Majorana states form when the den-

sity of states is large enough to support a well-formed superconducting gap. As the chemical potential moves past this onset value we find that the vortices are localized on the surfaces but hybridize with neighboring vortices on the same surface giving rise to a dispersive low-energy quasi-particle spectrum. As the chemical potential is pushed further into the bands, we find a critical chemical, μ_t, at which inter-surface tunneling is enabled through a gapless channel on the vortex line. The value is renormalized from that stated in Ref. 1, but we find that even for strong attractive interactions that μ_t remains at a finite value of the bulk-doping. After the chemical potential exceeds μ_t, we find that a gap opens in the spectrum and there are no longer any low-energy localized modes remaining. Additionally, in Section V, we evaluate the superconducting gap equation in order to determine the relevant temperature scale on which these effects may be observed. Finally, in Section VI we summarize our findings and conclude.

II. MODEL HAMILTONIAN OF A 3D TOPOLOGICAL INSULATOR

We will use a minimal, four-band Dirac-type model which, with the proper choice of parameter values, captures the bulk, low-energy physics of known TI materials such as Bi_2Se_3[40,41]:

$$H = \sum_{\vec{r}} \left\{ \Psi_{\vec{r}}^\dagger H_m \Psi_{\vec{r}} + \sum_{\vec{\delta}} \Psi_{\vec{r}}^\dagger H_{\vec{\delta}} \Psi_{\vec{r}+\vec{\delta}} \right\}, \quad (1)$$

$$H_m = \mathbb{M}\Gamma^0, \quad H_{\vec{\delta}} = \sum_{\vec{\delta}} \frac{b\Gamma^0 + i\gamma\vec{\delta}\cdot\vec{\Gamma}}{2a^2}, \quad (2)$$

where $\Psi_{\vec{r}} = (c_{A,\uparrow,\vec{r}} \; c_{A,\downarrow,\vec{r}} \; c_{B,\uparrow,\vec{r}} \; c_{B,\downarrow,\vec{r}})^T$ is a four-component spinor with A/B and $\uparrow / \downarrow$ labeling orbital and physical spin respectively so that $c_{\alpha,\sigma,\vec{r}}^\dagger$ is the creation operator for an electron with spin σ in orbital α at position $\vec{r}$, $\vec{\delta} = \pm a\hat{x}, \pm a\hat{y}, \pm a\hat{z}$ are vectors that connect nearest neighbors on a simple cubic lattice with lattice constant a, the vector $\vec{\Gamma} = \Gamma^x\hat{x} + \Gamma^y\hat{y} + \Gamma^z\hat{z}$ with $\Gamma^\alpha = \tau^x \otimes \sigma^\alpha$ and $\Gamma^0 = \tau^z \otimes \mathbb{I}$, where $\alpha = x, \; y, \; z; \; \tau^\alpha$ and σ^α are 2×2 Pauli matrices acting on orbital and spin degrees of freedom, respectively. We also define $\mathbb{I}$ as the 2×2 identity matrix and $\mathbb{M} = m - 3b/a^2$ as the mass parameter which controls the magnitude of the bulk band gap. The TI/trivial insulator phase depends on the chosen values for the parameters m and b and the TI phase has $m/b > 0$ while the trivial phase has $m/b < 0$. By tuning the material parameters $\gamma, b, m,$ and a in Eq. (1) one can model the low energy effective model for the common binary TI materials[40,41]. Since we only address the qualitative effects stemming from the TI phase we will fix the parameters to be $b = a^2(1eV)$, $\gamma = a(1eV)$ and $m = 1.5$ eV in terms of the lattice constant a so that $\mathbb{M} = -1.5$ eV thereby ensuring that we are in the TI phase.

With translation invariance and periodic boundary conditions in all x, y and z directions, it is often more convenient to work in momentum space. In this case, we expect to see no gapless states due to the lack of a boundary. The Fourier transformed Dirac Hamiltonian in momentum space may be written as

$$H = \sum_{\vec{k}} \Psi_{\vec{k}}^{\dagger} H_0(\vec{k}) \Psi_{\vec{k}}, \qquad (3)$$

where $H_0(\vec{k})$ in Eq. (3) is a 4×4 matrix which we may write as

$$H_0(\vec{k}) = \begin{pmatrix} \mathbb{M} + g(\vec{k}) & 0 & \sin k_z & \sin k_x - i \sin k_y \\ 0 & \mathbb{M} + g(\vec{k}) & \sin k_x + i \sin k_y & -\sin k_z \\ \sin k_z & \sin k_x - i \sin k_y & -[\mathbb{M} + g(\vec{k})] & 0 \\ \sin k_x + i \sin k_y & -\sin k_z & 0 & -[\mathbb{M} + g(\vec{k})] \end{pmatrix}, \qquad (4)$$

with $g(\vec{k}) = \cos k_x + \cos k_y + \cos k_z$. If we instead choose open boundaries along one direction there will be robust gapless edge states on those boundary surfaces for the same choice of model parameters.

III. TOPOLOGICAL INSULATORS WITH BULK S-WAVE SUPERCONDUCTIVITY

In this work, we are interested in the properties of doped TIs which become intrinsically superconducting at low temperature. In a doped topological insulator, like any other metal, when the chemical potential is in the conduction or valence band an attractive interaction will lead to the formation of superconductivity and generate a superconducting gap at the Fermi surface. In order to study the formation of superconductivity in doped TI we add an attractive Hubbard-type density-density interaction to the Hamiltonian in Eq. (1) :

$$H_{int} = -|U| \sum_{\vec{r}} n_{\uparrow,\vec{r}} n_{\downarrow,\vec{r}} \qquad (5)$$

where $n_{\sigma,\vec{r}} = c_{A,\sigma,\vec{r}}^{\dagger} c_{A,\sigma,\vec{r}} + c_{B,\sigma,\vec{r}}^{\dagger} c_{B,\sigma,\vec{r}}$ and the parameter $-|U|$ represents the attractive intra-orbital interaction.

At the mean-field level the interaction term may be decoupled as[42]:

$$-|U| \sum_{\alpha,\vec{r}} \left\{ \Delta_{\alpha,\vec{r}}^{*} c_{\alpha,\downarrow,\vec{r}} c_{\alpha,\uparrow,\vec{r}} + \Delta_{\alpha,\vec{r}} c_{\alpha,\uparrow,\vec{r}}^{\dagger} c_{\alpha,\downarrow,\vec{r}}^{\dagger} - |\Delta_{\alpha,\vec{r}}|^2 \right\},$$

where $\Delta_{\alpha,\vec{r}} = \langle c_{\alpha,\downarrow,\vec{r}} c_{\alpha,\uparrow,\vec{r}} \rangle$ is the standard intra-orbital s-wave pairing order parameter. Combining this with Eq. (1), we get the Bogoliubov-de Gennes (BdG) Hamiltonian:

$$H_{BdG} = \sum_{\vec{r}} \Phi_{\vec{r}}^{\dagger} \begin{pmatrix} H_m - \mu_{\vec{r}} & \Delta(\vec{r}) \\ \Delta(\vec{r})^{\dagger} & -H_m^* + \mu_{\vec{r}} \end{pmatrix} \Phi_{\vec{r}}$$

$$+ \sum_{\vec{r},\vec{\delta}} \Phi_{\vec{r}}^{\dagger} \begin{pmatrix} H_{\vec{\delta}} & 0 \\ 0 & -H_{\vec{\delta}}^* \end{pmatrix} \Phi_{\vec{r}+\vec{\delta}}, \qquad (6)$$

where $\Phi_{\vec{r}} = (\Psi_{\vec{r}}, \Psi_{\vec{r}}^{\dagger})^T$ is now an 8-component Nambu spinor, and $\Delta(\vec{r})$ denotes a 4×4 pairing matrix. In this expression, the interaction $-|U|$ has been absorbed into the pairing matrix $\Delta(\vec{r})$, which we write as

$$\Delta(\vec{r}) = -|U| \begin{pmatrix} 0 & \Delta_{A,\vec{r}} & 0 & 0 \\ -\Delta_{A,\vec{r}} & 0 & 0 & 0 \\ 0 & 0 & 0 & \Delta_{B,\vec{r}} \\ 0 & 0 & -\Delta_{B,\vec{r}} & 0 \end{pmatrix} \qquad (7)$$

To study the bulk superconductivity we will assume $\mu_{\vec{r}} = \mu$ is uniform throughout the material for simplicity.

The BdG Hamiltonian of Eq. (6) can be diagonalized by applying a Bogoliubov transformation as[42]

$$\begin{pmatrix} \Psi_{\vec{r}} \\ \Psi_{\vec{r}}^{\dagger} \end{pmatrix} = \sum_{n} \begin{pmatrix} u_{n,\vec{r}} & -v_{n,\vec{r}}^* \\ v_{n,\vec{r}} & u_{n,\vec{r}}^* \end{pmatrix} \begin{pmatrix} \gamma_n \\ \gamma_n^{\dagger} \end{pmatrix}, \qquad (8)$$

where n labels the eigenstate index. Plugging the transformation into Eq. (6), we have

$$H_{BdG} \sum_{n} \begin{pmatrix} u_{n,\vec{r}} & -v_{n,\vec{r}}^* \\ v_{n,\vec{r}} & u_{n,\vec{r}}^* \end{pmatrix}$$

$$= \sum_{n} \begin{pmatrix} E_n & 0 \\ 0 & -E_n \end{pmatrix} \begin{pmatrix} u_{n,\vec{r}} & -v_{n,\vec{r}}^* \\ v_{n,\vec{r}} & u_{n,\vec{r}}^* \end{pmatrix}. \qquad (9)$$

This indicates that the eigenvectors associated with E_n $(-E_n)$ of the above BdG equations are $(u_{n,\vec{r}}, v_{n,\vec{r}})^T$ $[(-v_{n,\vec{r}}^*, u_{n,\vec{r}}^*)^T]$. The mean-field pairing order parameters are obtained via

$$\Delta_{\alpha,\vec{r}} = \langle c_{\alpha,\downarrow,\vec{r}} c_{\alpha,\uparrow,\vec{r}} \rangle$$

$$= \sum_{n} u_{n,\vec{r}} v_{n,\vec{r}}^* \tanh \frac{\beta E_n}{2}, \qquad (10)$$

where $\beta = 1/k_B T$. Once the pairing order parameter are determined initially it is plugged back into the BdG Hamiltonian given in Eq. (6) and then H_{BdG} is diagonalized again as shown in Eq. (9). The process continues until we reach self-consistency and we have a convergent $\Delta_{\alpha,\vec{r}}$ for all $\vec{r}$. We note that in our numerical calculations we use a small, non-zero temperature in order to avoid
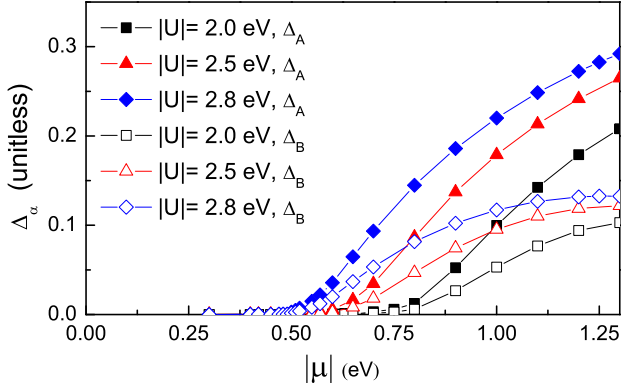
FIG. 1. (color online). Intra-orbital pairing order parameters Δ_A (solid symbols) and Δ_B (hollow symbols) vs $|\mu|$ at different $|U|$. $|\mu|$ and $|U|$ are in units of eV. Via our definition for pairing in Eq. (10), Δ remains unitless. The mass term $\mathbb{M} = -1.5$ eV. The system contains periodic boundary conditions in x, y and z directions. The simulations are performed on a lattice grid of size $80a \times 80a \times 10a$.

divergences but this temperature is much smaller than the superconducting gap so as not to affect the physical results.

In Fig. 1 we show the self-consistently determined intra-orbital pairing order parameter in the bulk as a function of $|\mu|$ at different $|U|$, where, due to translation invariance, $\Delta_{\alpha,\vec{r}} = \Delta_\alpha$. In this paper we will only consider p-doping ($\mu < 0$), but the particle-hole symmetry of the model Hamiltonian in Eq. (1) makes the electron-doped case similar in nature. With $\mathbb{M} = -1.5$ eV in Eq. (1), the top of the bulk valence band is located at $\mu_v = -0.5$ eV and the total size of the insulating gap is 1.0 eV. We see from Fig. 1 that when the chemical potential is in the gap where there is no carrier density with which to form Cooper pairs and the resulting pairing potential is zero. When the chemical potential enters the valence band a Fermi-surface develops, and low-energy states become available to pair. However, when the density of states at the Fermi-level is insufficient, the size of the pairing potential will continue to be exponentially small. As we see in Fig. 1, a significant pairing potential does not form until $|\mu|$ is well above the valence band edge, $|\mu_v|$.

This result matches standard BCS phenomenology and represents the point of inception for the remainder of the paper. To be specific, in Ref. 1 Hosur et al. used a semi-classical treatment to show that a vortex in the superconducting phase of a doped topological insulator exhibits a topological phase transition as the chemical potential is tuned through a critical value. The two phases separated by this transition are gapped and differ by the presence or absence of Majorana modes at the ends of the vortex *i.e.* where the vortex line intersects the surface of the TI. At the transition point the vortex line becomes gapless and provides a channel which allows the Majorana modes to annihilate one another by tunneling in-between the op-

posing surfaces. In their treatment, however, there is an assumption of adiabaticity (i.e. the continuous transformation of the system Hamiltonian from insulating state into the superconducting state without closing the band gap) as it is always assumed that at any chemical potential other than the critical chemical potential, there is no gapless channel to hybridize the Majorana mode. This seems innocuous, but one has to remember that the arguments rely on the adiabatic connection between a gapped insulating phase and a gapped superconducting phase. This assumption becomes important when one considers the behavior of the system as the chemical leaves the insulating gap and enters the bulk bands. Although this is a reasonable assumption within which to theoretically study the vortex phase transition, one may then ask what happens in the region where the chemical potential is not large enough to form a significant pairing potential, and there is finite density of gapless modes in the bulk. In other words, how does the Majorana mode emerge out of the bulk gapless states? This question is certainly relevant for experiments where a finite size TI sample is used. Our self-consistent solution of the BdG equations in the vortex lattice in the strong-pairing limit (i.e. when the magnitude of attractive potential is comparable with the band width) can present a clearer picture of the appearance of the Majorana modes and the vortex phase transition than the previous semi-classical analysis.

IV. VORTEX LATTICES IN SUPERCONDUCTING PHASE OF DOPED TOPOLOGICAL INSULATORS

The self-consistent BdG formalism is in a real space basis and thus can be also used to study the vortices in the superconducting phase where the order parameter will be non-uniform. To induce vortices, we consider the system under a uniform magnetic field $\vec{B} = B\hat{z}$. When electrons are hopping on the xy-plane this generates a Peierls phase factor, and the BdG Hamiltonian becomes[34,43]

$$H_{BdG} = \sum_{\vec{r}} \Phi_{\vec{r}}^\dagger \begin{pmatrix} H_m - \mu_{\vec{r}} & \Delta(\vec{r}) \\ \Delta^\dagger(\vec{r}) & -H_m^* + \mu_{\vec{r}} \end{pmatrix} \Phi_{\vec{r}}$$
$$+ \sum_{\vec{r},\delta} \Phi_{\vec{r}}^\dagger \begin{pmatrix} H_\delta e^{-i\eta_{\vec{r}}} & 0 \\ 0 & -H_\delta^* e^{i\eta_{\vec{r}}} \end{pmatrix} \Phi_{\vec{r}+\delta}$$

$$(11)$$

where $\eta_{\vec{r}}$ denotes the extra phase given by the vector potential $\vec{A}(\vec{r})$ induced by the magnetic field through $\vec{B} = \nabla \times A(\vec{r})$:

$$\eta_{\vec{r}} = \frac{\pi}{\Phi_0} \int_{\vec{r}}^{\vec{r}+\delta} \vec{A}_{\vec{r}'} \cdot d\vec{r}', \qquad (12)$$

where Φ_0 is the superconducting flux quantum; $\Phi_0 = \frac{h}{2e}$. In the following discussion, we choose the Landau gauge, i.e. $\vec{A}(\vec{r}) = (A_x, A_y) = (0, Bx)$.
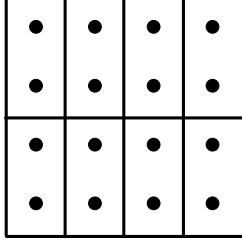
FIG. 2. A 4×4 vortex lattice. In this example, the number of magnetic unit cells is $N_x \times N_y = 4 \times 2$. Each black solid circle denotes a vortex location and each magnetic unit cell contains two vortices.

We will treat the system as a type-II superconductor in a vortex lattice state. In each magnetic unit cell, the amount of magnetic flux is $2\Phi_0$, so that each unit cell carries two superconducting vortices[44]. We designate the size of each magnetic unit cell as $l_x a \times l_y a \times l_z a$ using the integers l_i to denote the number of lattice sites in each spatial direction. For our choice of geometry we will use square vortex lattices, and fix $l_x = l_y/2$. The corresponding magnetic field magnitude is

$$B = \frac{2\Phi_0}{l_x l_y a^2}. \tag{13}$$

From this relation we can observe that stronger magnetic fields bring smaller magnetic unit cells, in which vortices are closer each other. Therefore, the dilute vortex limit comes from applying very weak magnetic fields. As is standard for lattice calculations with uniform field, in order to see experimentally reasonable field sizes we would need to use a very large number of unit cells as, for example, the case when $l_x = l_y = 1$ gives a magnetic field on the order of thousands of Tesla. For our system sizes we have an un-physically large magnetic field on the order of 10^3 T assuming a lattice constant of $1 \mathring{A}$. This, however, will not affect the qualitative physics in which we are interested and we will not worry about this issue any further.

We choose the entire system size as $L_x a \times L_y a \times l_z a$ such that there are $N_x \times N_y$ magnetic unit cells, where $N_x = L_x/l_x$ and $N_y = L_y/l_y$ and $N_x = 2N_y$. Since each magnetic unit cell carries two vortices, the $L_x a \times L_y a \times l_z a$ vortex lattice contains $2N_x N_y$ vortices. In Fig. 2, we show a schematic illustration of a 4×4 square vortex lattice. By tuning sizes of the magnetic unit cells, we can study the vortex lattice at different external magnetic fields. In this paper, we set $l_x > 8$ to avoid strong overlap between vortices but $l_x \leq 12$ due to computational limitations.

We consider a system with periodic boundary conditions along the x and y directions. Although the vortices break lattice translation invariance, we still have magnetic periodic boundary conditions for vortex lattices. In addition to the phases given by vector potentials $e^{i\eta_{\vec{r}}}$, the magnetic periodic boundary conditions also contribute another phase factor when electrons are hopping across unit cell boundaries[45,46]. Suppose that in a 2D vortex lattice, the translation vector in units of a is written as $\vec{R} = (Xl_x, Yl_y)$, where $X = 0, \cdots, N_x - 1$ and $Y = 0, \cdots, N_y - 1$ are integers. The coordinate of an arbitrary lattice site can be expressed as $\vec{r} + \vec{R}$, where $\vec{r} = (x, y)$ denotes the coordinate in units of the lattice site, a, within a magnetic unit cell, i.e. $1 \leq x \leq l_x$ and $1 \leq y \leq l_y$. Under the magnetic periodic boundary conditions, we can define the relation of the magnetic Bloch wave functions[47] which have a periodic structure written as[47,48]

$$\begin{pmatrix} u_n(\vec{r} + l_x \hat{x}) \\ v_n(\vec{r} + l_x \hat{x}) \end{pmatrix} = e^{ik_x} \begin{pmatrix} e^{2\pi i \frac{y}{l_y}} u_n(\vec{r}) \\ e^{-2\pi i \frac{y}{l_y}} v_n(\vec{r}) \end{pmatrix},$$

$$\begin{pmatrix} u_n(\vec{r} + l_y \hat{y}) \\ v_n(\vec{r} + l_y \hat{y}) \end{pmatrix} = e^{ik_y} \begin{pmatrix} u_n(\vec{r}) \\ v_n(\vec{r}) \end{pmatrix}. \tag{14}$$

Here $k_x = \frac{2\pi X}{N_x}$ and $k_y = \frac{2\pi Y}{N_y}$ represent the x and y components of the magnetic Bloch wavevector. The phases e^{ik_x} and e^{ik_y} arise from hopping to neighboring cells. Additionally, $e^{\pm 2\pi i \frac{y}{l_y}}$ is provided by the magnetic periodic boundary conditions, or quasi-periodic boundary conditions[47]. The BdG eigenstates $(u_{n,\vec{r}}, v_{n,\vec{r}})^T$ satisfy magnetic translation invariance under Eq. (14).

The on-site pairing potential can be expressed as $\Delta_{\alpha,\vec{r}} = |\Delta_{\alpha,\vec{r}}| e^{i\phi(\vec{r})}$ with a phase $e^{i\phi(\vec{r})}$ and amplitude $|\Delta_{\alpha,\vec{r}}|$. In the presence of vortices, both the pairing potential and the phase are site-dependent. The superconducting order parameters are suppressed near the vortex cores, and are restored to the bulk values away from the vortex cores. The spatial form of the pairing order parameters $\Delta_{\alpha,\vec{r}}$ are determined self-consistently. We consider different attractive-Hubbard interaction strengths $|U|$ and uniform doping-levels $|\mu|$ distributed through the entire bulk.

We study two different geometries for the vortex lattice. First we consider vortices oriented in the z-direction (along the applied magnetic field) with periodic boundary conditions along the x, y, z directions which yields vortex rings looping around the z-direction. In this geometry we study the vortex phase transition where the vortex modes become gapless along the vortex rings. The second geometry we consider has open boundaries in the z-direction. In this case the vortex lines terminate at the open surfaces perpendicular to the z-axis and we can study the Majorana modes that can appear at the vortex ends in the topological phase. We compare these results, which are neither in the semi-classical, or infinitesimally weak-pairing limits, to the results studied in Ref. 1 which are in these limits.

A. Periodic Vortex Rings in Vortex Lattices

With periodic boundary conditions in all spatial directions, we cannot directly study the Majorana modes that might appear at the vortex ends. However, we can indi-
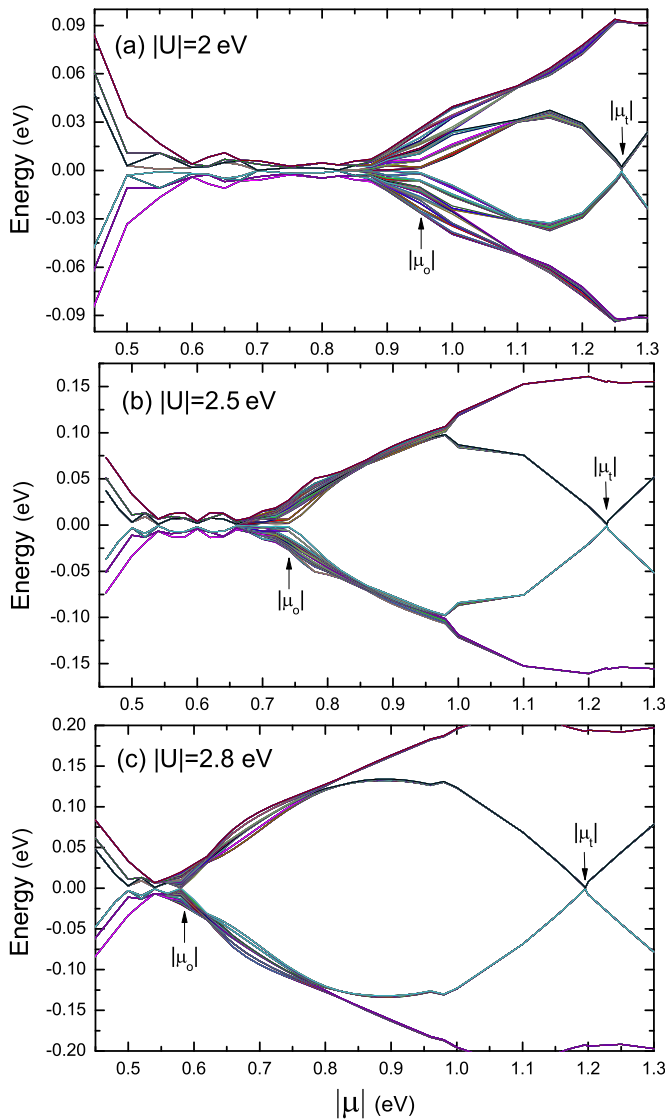
FIG. 3. (color online). The energy spectra of the low-energy states vs $|\mu|$ for periodic boundary conditions along the z-axis (vortex rings) for (a) $|U| = 2$ eV, (b) $|U| = 2.5$ eV, and (c) $|U| = 2.8$ eV. The systems have a $N_x \times N_y = 10 \times 5$ (100 vortices) vortex lattice and the size of the magnetic unit cell is $l_x \times l_y \times l_z = 12a \times 24a \times 10a$. We note that in this work, we assume that the Zeeman splitting due to the applied magnetic field is negligible.

rectly study them by identifying the vortex phase transition through a study of the low-energy modes along the vortex lines. As the chemical potential is tuned deeper into the band, the point where one of these modes becomes gapless signals the location of a critical point. For this geometry the magnetic unit cell sizes we use are $l_x \times l_y \times l_z = 12 \times 24 \times 10$. We choose $N_x \times N_y = 10 \times 5$ unit cells so that there are 100 vortices in the vortex lattice.

In Fig. 3, we present the evolutions of the low energy states vs $|\mu|$ for different interaction strengths $|U|$. We can identify two distinctly different doping regimes. In

the first regime, the chemical potential lies in the valence band but below a value we call $|\mu_o|$ which signals the onset of a well-formed superconducting gap discerned from our numerics. It should be noted that $|\mu_o|$ has no real intrinsic meaning (as it is strongly finite-size dependent) and only serves to indicate a common feature shared by all of our spectrum plots. Clearly, before the chemical potential hits the top of valence band there is no density of states to generate the superconducting gap, and all the states are gapped by the bulk insulating band gap. After the chemical potential hits the top of valence band, the superconducting pairing starts to form but it is exponentially small in magnitude. Comparing the pairing strengths without vortices (i.e. Fig. 1) to the vortex lattice case in Fig. 3, our numerics show that in the vortex lattice the pairing is more poorly formed over a larger range of doping. That is, the states at the Fermi level remain gapless with no superconducting gap formation. Note that μ_o decreases with increasing $|U|$ which indicates that this point is sensitive to the point where the exponentially suppressed superconducting gap would turn on. In this regime, any localized Majorana modes or low-energy vortex core states are difficult to distinguish from the extended gapless metallic states in the bulk. The details of this regime are dominated by strong finite-size effects. One hindrance is that for cases where only a tiny pairing potential would form it is numerically challenging to generate a convergent, self-consistent solution with vortices present. In the thermodynamic limit, we would expect to see a non-zero but exponentially small pairing gap as soon as the chemical potential hits the valence band. Here the situation is not so clear, and unfortunately, due to the computational limitations, we cannot glean a great deal of physical information from this regime except that it is not obvious that the picture of an "adiabatic" continuation from the gapped insulating state immediately to a gapped superconducting state would be valid in a real sample. We will attempt to address this issue from another direction by studying a heterostructure geometry in Section IV C in which we can generate a convergent, vortex lattice solution by inhomogeneously doping the system i.e. high-doping on the surface and low-doping in the bulk.

In the second distinct regime, once $|\mu|$ is tuned beyond $|\mu_o|$, then significant s-wave pairing begins to develop. Because of the particle-hole constraint of the BdG quasiparticle spectrum, the energies appear in $\pm E$ pairs. The lowest energy branches are nearly $2 \times N_x \times N_y$ fold degenerate. This degeneracy clearly indicates that these states are in-gap vortex states as there is essentially one for each vortex. As the chemical potential is pushed more into the valence band, the lowest energy branch approaches zero energy and at critical chemical potential $|\mu_t|$, the particle and hole branches cross indicating the location of the vortex phase transition. In the weak-pairing treatment the critical chemical potential is independent of the value of the attractive potential $|U|$ and if we repeat their analysis for our choice of parameters, we find

a weak-pairing estimate of $|\mu_t| = 1.35$ eV. In our case, as the interaction strength is quite large we are not in the weak-pairing limit and the critical chemical potential depends on the attractive potential. At $|U| = 2$ eV, 2.5 eV and 2.8 eV, $|\mu_t| \simeq 1.26$ eV, 1.22 eV and 1.2 eV, respectively. A stronger $|U|$ gives a smaller value of $|\mu_t|$ and it approaches to the weak paring limit as we decrease the magnitude of interaction. Since the phenomenon survives the weak-pairing limit it is possible that the vortex topological phase transition could also be observed in a strong-pairing atomic limit which is realizable in ultra-cold optical lattices[49].

In Fig. 4, we show the self-consistent vortex profiles in a single unit cell as a function of $|\mu|$ for $|U| = 2.8$ eV. It is evident that in all cases around the vortex cores, the pairing order parameters are suppressed. Away from the vortex cores the pairing order parameters are restored to $\Delta_A = 0.21$, 0.213 and 0.29 which are roughly equal to the corresponding bulk values at $|\mu| = 0.96$ eV, 0.98 eV and 1.3 eV respectively (c.f. Fig. 1). In the bulk superconducting TI, at larger $|\mu|$ stronger Cooper pairing is induced, and the strong superconductivity leads to a shorter coherence length ξ_0 ($\xi_0 = \frac{\hbar v_F}{\pi \Delta}$),[42] and thus a smaller vortex size. Therefore, in Fig. 4(b) and (c), we see flatter order parameter profiles. However, we find unusual behavior in these figures associated with chemical potentials of $|\mu| = 0.98$ eV and 1.3 eV. At these chemical potentials, the vortices do not seem to be as well formed as they are when $|\mu| = 0.96$ eV. This is due to the numerical discreteness in our simulations. In our system, because of the non-trivial order parameter winding due to the vortex, there *must* be a place where the order parameter magnitude vanishes. One can see that in Fig. 4 this only happens for $|\mu| = 0.96$. What is happening is that the vortex core moves from being centered at a lattice vertex to the interior of a plaquette. The order parameter then vanishes in the plaquette interior (which of course is not seen on our discrete lattice spatial sampling). In fact, we find that at particular values of the chemical potential it becomes energetically favorable for the vortex to move its core off of a lattice vertex and into the center of a plaquette. This is seen in the energy spectra in Fig. 3 where we a kink in the spectrum a appears where this vortex shift occurs, namely around $|\mu_k| = 0.97$ eV. We believe this is simply an artifact of our numerical technique and does not represent any real physics.
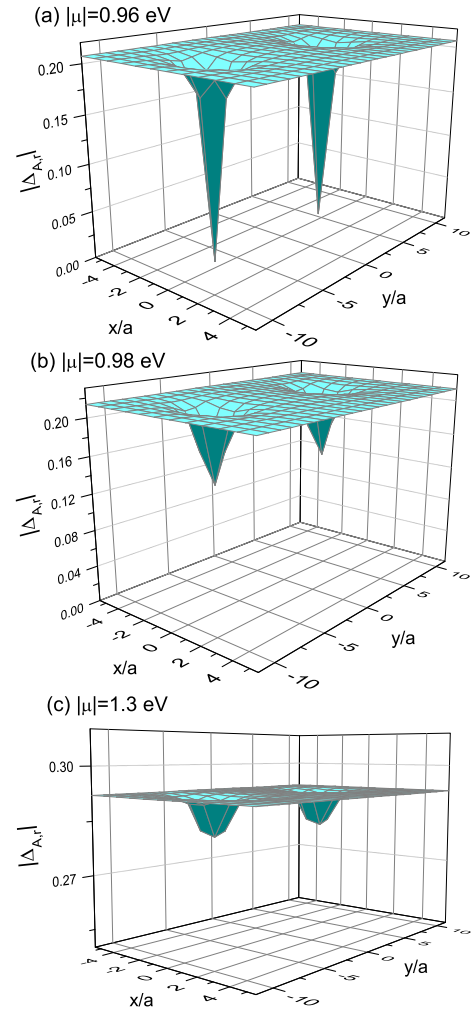

FIG. 4. (color online). The spatial pairing order parameter profiles $|\Delta_{A,\vec{r}}|$ within a unit cell at $|U| = 2.8$ eV and at (a) $|\mu| = 0.96$ eV (b) $|\mu| = 0.98$ eV and (c) $|\mu| = 1.3$ eV. The vertical axis represents the pairing order parameter magnitudes and the horizontal plane is xy plane. Note the variation of the pairing order parameter magnitudes at the unit cell center $\Delta_{\text{center}} = \Delta_{A,\vec{r} \in \text{unit cell center}}$ for different μ: (a) $\Delta_{\text{center}} \simeq 0$, (b) $\Delta_{\text{center}} \simeq 0.12$, and (c) $\Delta_{\text{center}} \simeq 0.28$. $\Delta_{\text{center}} \simeq 0$ indicates that the vortex core stays on-site, whereas $\Delta_{\text{center}} \neq 0$ means that the vortex core moves off the lattice vertices and into the plaquette. We note that the profiles for $|\Delta_{B,\vec{r}}|$ look similar.

B. Open Vortex Lines in Vortex Lattices

Next we turn to the case with open boundary conditions along the z-direction such that the vortices terminate on the surfaces. This setting is directly relevant for possible experiments where the Majorana vortex modes are present at the end of vortex lines. Due to the open boundaries, the self-consistent BdG calculations must be performed in three spatial dimensions as we cannot exploit any translation symmetry in z direction. The mag-

netic unit cells are $l_x \times l_y = 8 \times 16$ sized with l_z-layers, (usually $l_z = 6$) and there are $N_x \times N_y = 40 \times 20$ magnetic unit cells chosen so that we are simulating 1600 vortices in the vortex lattice. In this section, we only consider $|U| = 2.8$ eV and $|\mu| > |\mu_o|$ where the superconducting gap is formed and the value of $|\mu_o|$ is estimated from the periodic boundary condition case. Here, we self-consistently determine the BdG quasi-particle spectrum in the vortex lattice state[43,47,50]. For the square vortex lattice with $N_x \times N_y$ magnetic unit cells, there are $N_x N_y$ magnetic Bloch wavevectors $\vec{k}$ analogous to the wavevec-
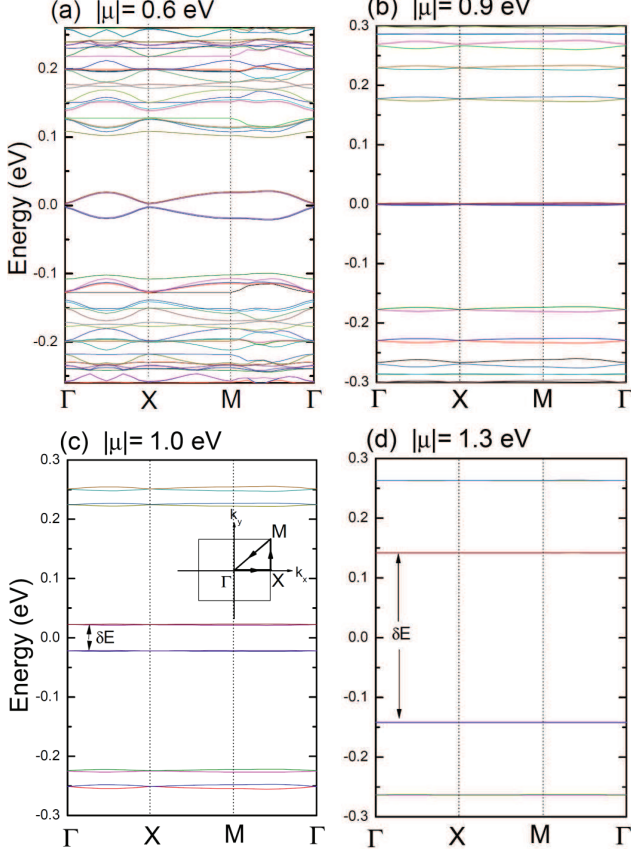
FIG. 6. (color online). The energy splitting δE vs thickness l_z. The magnetic unit cells are $8 \times 16 \times l_z$ at $|\mu| = 1$ eV and $|\mu| = 1.1$ eV. The Hubbard interaction is $|U| = 2.8$ eV.

conducting gap is formed, it remains small and the vortex modes of different vortices on the *same* surface can tunnel laterally and hybridize which leads to the dispersion of the vortex core states. As we increase the doping level, the lowest energy quasiparticle band flattens as is clear in the dispersion plot for $|\mu| = 0.9$ eV in Fig. 5(b). This happens because of the increasing bulk superconducting gap, indicated in Fig. 3(c). The vortex core size shrinks which leads to smaller overlap of the modes localized in different vortices and suppresses the quasiparticle dispersion. This effect (*i.e.* increase of superconducting gap by increasing the doping) stabilizes the Majorana modes. The low-energy, flat quasi-particle bands contain $4N_x N_y$ nearly-degenerate states coming from the $2N_x N_y$ vortex Majorana modes on the two distinct surfaces.

In Fig. 5, we see two clear gap-like behaviors. One type in Fig. 5(a) shows gaps at low-energy but with strong dispersion while Fig. 5(c) and (d) show clear gaps but with flat dispersion. For the flat-dispersing cases we studied the dependence of the energy splitting, δE, on the sample thickness. An exponential dependence would indicate that the dispersionless gap is a result of the hybridization of the modes at the end of the vortices between two surfaces. Fig. 6 shows the energy splitting δE has an exponential decreasing relation with the thickness l_z described as[4]

$$\delta E \propto e^{-\frac{l_z}{\xi_m}}, \qquad (15)$$

where ξ_m denotes the characteristic decay length for the Majorana modes. A smaller ξ_m means more localized Majorana bound states. By linear fitting from Fig. 6, the characteristic length at $|\mu| = 1$ eV is $\xi_m \simeq 5.46a$ and at $|\mu| = 1.1$ eV is $\xi_m \simeq 9.49a$. This suggests that the Majorana modes are still exponentially localized on the surface even though there is a gap in our finite-size numerics. Therefore, although the Majorana modes may tunnel to the opposite surface, in the thermodynamic limit ($l_z \to \infty$), the Majorana modes are still be bound to the surface. Although we do not show it here, we note

FIG. 5. (color online). The quasiparticle band structure for open vortex lines in the bulk superconducting TI. The interaction strength is chosen at $|U| = 2.8$ eV and the chemical potentials are (a) $|\mu| = 0.6$ eV, (b) $|\mu| = 0.9$ eV, (c) $|\mu| = 1.0$ eV and (d) $|\mu| = 1.3$ eV. The inset in (c) denotes the magnetic Brillouin zone for the square vortex lattice. The magnetic unit cell sizes are $l_x \times l_y \times l_z = 8a \times 16a \times 6a$.

tors in the Brillouin zone of a $\times N_x \times N_y$ square lattice.

In Fig. 5, we present the dispersion of vortex modes at four different chemical potentials as has been done previously for s-wave and d-wave superconductors[43,50]. The high symmetry points of the square lattice are at $\Gamma = (0,0)$, $X = (\pi, 0)$ and $M = (\pi, \pi)$, as indicated in the inset of Fig. 5(c). There are four low-energy "Majorana" modes at each momentum which are contributed by the two-vortices per cell and the two ends of each vortex line. For a single magnetic unit cell we would thus expect to see one Majorana mode on the two ends of each of the two vortex lines giving rise to a total of four vortices per cell. In this context, we put the word Majorana in quotes because, strictly speaking, the low-lying energy states only have true Majorana character if they are strictly at zero-energy. In Fig. 5(a), we study the quasiparticle bands at $|\mu| = 0.6$ eV and we find that the vortex modes are clearly dispersing. Although the super-
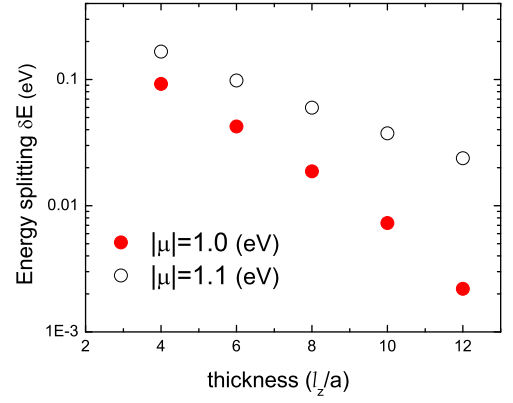
that this is not the case for $|\mu| = 1.3$ eV where the gap does not decrease exponentially, which is expected since this is the trivial regime where it should have a power-law decay with inverse thickness due to finite-size splitting.

The nature of the Majorana modes may be further illustrated by studying real space probability distributions of the in-gap modes. Fig. 7(a)-(d) depict side-view spatial slices of the probability density for the lowest energy modes and Figs. 7(e)-(h) show the order parameter distributions in real space. The plots are cut on the yz surface at $x = \pm 2a$, where the vortex cores are approximately located. The Majorana modes (indicated by bright regions) are observed and localized around the vortex cores close to the surfaces in Figs. 7(a) and (b). However, the Majorana mode in Fig. 7(a) spreads more widely along the surface than that in Fig. 7(b). This shows that at $|\mu| = 0.6$ eV neighboring vortices have larger overlap than that at $|\mu| = 0.9$ eV, which corroborates with our quasiparticle spectra that indicate stronger dispersion for the former case as shown in Fig. 5(a) due to the intra-surface hybridization resulting from the increased lateral overlap of the Majorana modes. It is also interesting to see that around $|\mu| = 0.9$ eV, the mini-gap size of the vortex lines is maximum, [see Fig. 3(c)] which is where and Fig. 7(f) shows strong, straight-line vortex structures.

At first, further increases in the chemical potential flattens the dispersion and strengthens the localization of the Majorana modes. However, further increases in the chemical potential lead to another tunneling mechanism for the Majorana modes. As we have already shown for periodic vortex rings (e.g see Fig. 3(c) as $|\mu| > 1$) the mini-gap of the vortex core states along the vortex line eventually begins to decrease as the critical point is approached. For open-boundary conditions this leads to increased inter-surface hybridization of the modes at the two ends of the vortex lines. This results in the formation of gaps due to Majorana mode annihilation on opposite surfaces (for thin samples) and in Fig. 5(c) we can see that there exists a δE splitting in the Majorana modes. As mentioned and shown in Fig. 6 δE decreases exponentially in the thickness of the sample. An important feature to note is that, as is clear from the dispersion for $|\mu| = 0.9$ eV, even though the gap increases the bandwidth of quasiparticles decreases and gets flatter. This is an indication that intra-surface tunneling is weakening (no 2D hopping on the same surface) and that inter-surface tunneling is becoming stronger. We can see this in Fig. 7(c), where the Majorana bound states begin to leak to the opposite surface. Furthermore, in Fig. 7 (d), in which case the system is topologically trivial, the lowest energy modes, which are no longer Majorana in nature and gapped by the vortex mini-gap of order Δ^2/μ, completely penetrate through the bulk at $|\mu| = 1.3$ eV and lie along the vortex lines.

C. Superconductor-Topological Insulator Heterostructure

As mentioned in the introduction, another method to realize the Majorana modes is through the proximity effect of a topological insulator and an s-wave superconductor. Using our self-consistent BdG method, we can also study this geometry. By modeling such a structure by an inhomogenous doping level we can directly address the effect of the penetration of superconducting gap into the bulk and the self-consistent formation of Majorana bound states in vortices. We imagine a similar proximity-induced superconductivity as was first suggested by Fu and Kane[16]. We choose an inhomogenous system where $\mu(\vec{r})$ in Eq. (11) is layer-dependent. We choose the surface chemical potential $\mu(\vec{r}) = \mu_S = -1$ eV, and the chemical potential $\mu(\vec{r}) = \mu_B = -0.55$ eV in other bulk layers so that both the bulk and surface have non-zero density of states. We investigate the case where superconductivity is induced primarily on the surfaces by turning on the same attractive interaction across the entire sample. The inhomogeneous $\mu(\vec{r})$ will generate a much stronger order parameter on the surfaces than in the bulk due to the large difference in chemical potentials. Again we choose a uniform magnetic field along the z-direction which generates the vortex lattice.

There is another reason to consider this system beyond simply the presence of Majorana fermions. One of the major obstacles in our bulk calculation is the non-convergence of a stable vortex solution when the order parameter magnitude is very small. As mentioned, when $|\mu_v| < |\mu| < |\mu_o|$ despite the presence of gapless electrons at the Fermi-level, the density of states is not large enough to form a sizable superconducting gap (at least for system sizes we consider) and the doped TI remains a gapless metal. We can counter-act this problem by using the superconductor-TI heterostructure geometry which acts to pin the vortices with strong superconductivity at the surface (highly-doped region) thereby stabilizing the solution. Fig. 8 shows the spatial side view of the resulting self-consistent order parameter profile of a six-layer heterostructure. We see no evidence of superconductivity in the bulk and roughly uniform superconductivity in the surface which is interrupted near the vortices. The resulting calculation in Fig. 9b shows that Majorana surface modes still remain even though the superconducting order parameter in the bulk is exponentially small compared to the surface. The six-layer heterostructure can roughly approximate the case of two vortices existing in a four-layer bulk TI which is *uniformly* doped with $|\mu| = 0.55$ eV. This was a region of interest that we could not access in our bulk calculation due to finite-size complications and which we can, admittedly only roughly, learn about by stabilizing the vortex solution using higher surface doping.

In Fig. 9(a), we present the quasi-particle band spectrum for the superconductor-TI heterostructure with a square vortex lattice. Within the superconducting gap,
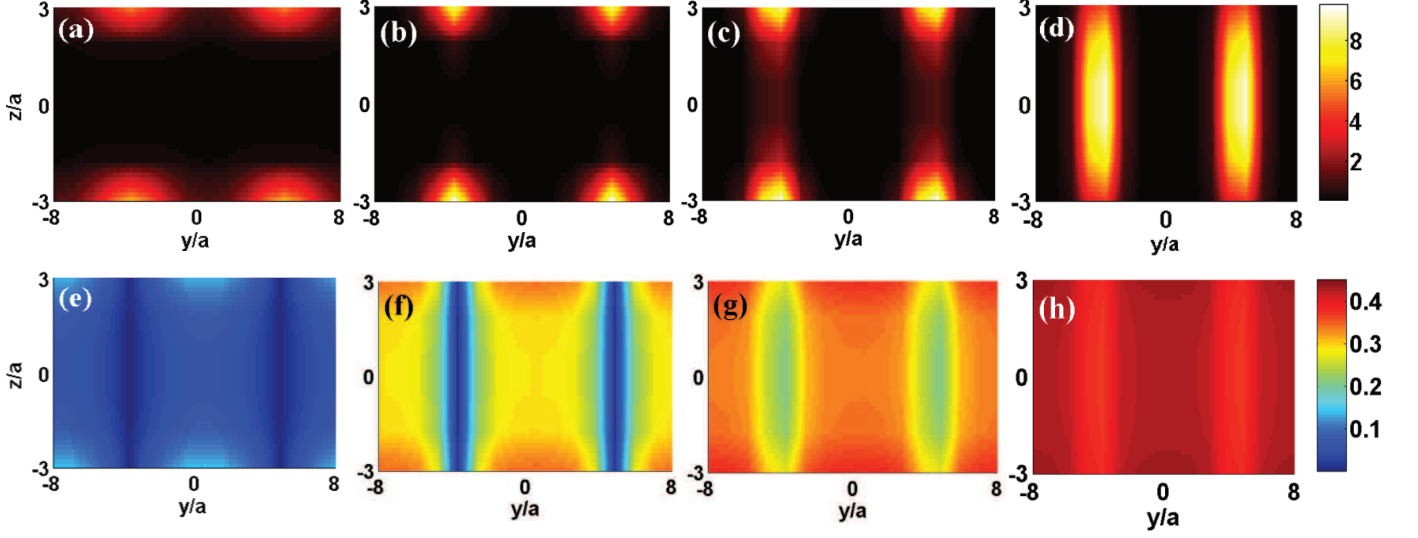
FIG. 7. (color online). Spatial slices (side-views in the yz plane at $x = \pm 2a$) of the probability density for the Majorana modes and order parameter density in the bulk superconducting TI at different μ. Upper panels: (a)-(d) shows the evolution of the Majorana mode distributions. Brighter regions represent the higher probability density. Lower panels: (e)-(h) shows the distribution of pairing order parameters ($|\Delta_A + \Delta_B|$). The chemical potentials are $|\mu| = 0.6$ eV in (a) and (e), $|\mu| = 0.9$ eV in (b) and (f), $|\mu| = 1$ eV in (c) and (g), and $|\mu| = 1.3$ eV in (d) and (h), respectively.
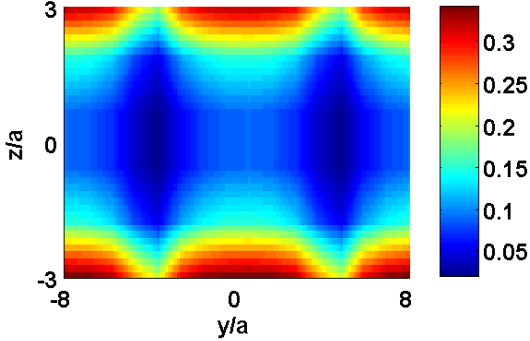
FIG. 8. (color online). The spatial side view of the pairing order parameter distribution of a six-layer the s-wave/TI heterostructure. The interaction strength is chosen at $|U| = 2.8$ eV, and the surface and bulk chemical potentials are $|\mu_S| = 1$ eV and $|\mu_B| = 0.55$ eV, respectively. The dark blue tubes indicate the region that pairing is suppressed and form vortex lines. The magnetic unit cell sizes are $8a \times 16a \times 6a$

there exist two prominent low-energy modes which are doubly degenerate whose energies are split away from zero energy. Although not shown here, we find that the energy splitting δE also has an exponential decay with increasing sample thickness l_z. This indicates that the low-energy modes are exponentially localized at the superconducting surface and the Majorana fermions can stably reside at the surfaces in the thermodynamic limit, i.e. $l_z \to \infty$. This is indicative that that the vortices in the low-doping regime ($|\mu_v| < |\mu| < |\mu_o|$) also support Majorana fermions in the bulk superconducting TI. In Fig. 9(b) we show the probability density of the low en-

ergy modes and see the tight localization of the resulting modes on the surface as one would expect for Majorana modes formed within a well-formed superconducting gap.

V. VORTEX MAJORANA MODES AT FINITE TEMPERATURES

In our previous analysis, we have neglected the role of temperature in our analysis. In this section, we provide a rough estimate of the temperature at which one could observe the Majorana fermions experimentally. In the BCS theory the temperature dependence of the gap size is determined through:[42]

$$\frac{1}{N(0)V} = \int_0^{\hbar \omega_c} \frac{\tanh\left[\frac{\sqrt{\xi^2 + \Delta(T)^2}}{2k_B T}\right]}{\sqrt{\xi^2 + \Delta(T)^2}} d\xi. \quad (16)$$

Here $N(0)$ is the density of states at the Fermi-level, U is the interaction coupling, and ω_c is the Debye frequency. The finite temperature gap $\Delta(T)$ may only be determined numerically. The combination of $N(0)U$ can be estimated from the critical temperature, T_c, and the Debye frequency, ω_c, for Cu-doped Bi_2Se_3 via:

$$N(0)U = \frac{-1}{\ln\left[\frac{k_B T_c}{1.13 \hbar \omega_c}\right]}. \quad (17)$$

For Bi_2Se_3, the critical temperature is $T_c = 3.8$K,[36,37] and the Debye temperature $\hbar \omega_c / k_B$ is 180 K[51]. With

FIG. 10. (color online) The comparison between the midgap sizes $\delta_m(T)$ and $k_B T$. The intersection occurs at $T = T_0 \sim 0.025$ K indicating that as $T < T_0$, the Majorana modes can stably exist on the surface of the doped topological insulators.
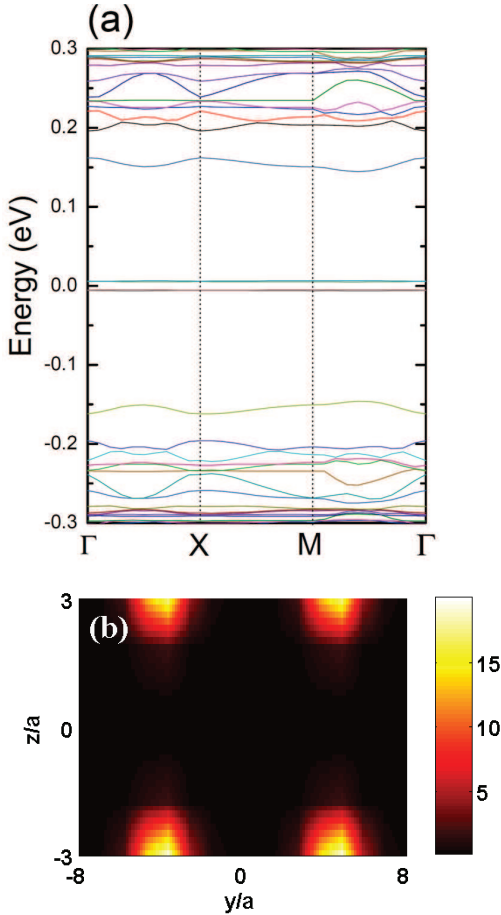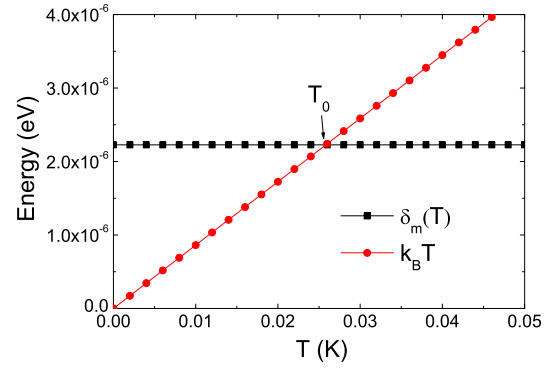

FIG. 9. (color online). (a) The quasiparticle band spectrum for six-layer the s-wave/TI heterostructure. (b) The spatial side view of the Majorana modes. The interaction strength is chosen at $|U| = 2.8$ eV and $|\mu_S| = 1$ eV and $|\mu_B| = 0.55$ eV.

$N(0)U$ determined from Eq. (17), one can calculate the temperature dependence of the gap numerically using Eq. (16). To observe the Majorana modes at finite temperature, the mini-gap size of the vortex lines $\delta_m(T)$ should be stable against the thermal fluctuations: $\delta_m(T) < k_B T$. The temperature at which this occurs may be estimated as

$$T_0 = \frac{\delta_m(T)}{k_B} = \frac{\pi \Delta(T)^2}{2 k_B \delta \varepsilon_F}, \qquad (18)$$

where $\delta \varepsilon_F = |\mu - \mu_b|$ where μ_b denotes the bulk band edge. When $T < T_0$, the Majorana modes can stably exist on the surfaces and can be detected experimentally. The numerical result is shown in Fig. 10. From Ref. 52, in Bi_2Se_3, $\delta \varepsilon_F \sim 0.25$ eV which results in an estimate for the critical temperature for the observation of Majorana modes to be $T_0 \sim 0.025$ K. Therefore, we can provide a rough estimate that at $T \lesssim 0.025$ K, the Majorana modes can stably exist on the surface of the doped topological insulators and may be detectable experimentally. This number is quite small and indicates one would need to optimize materials properties in order to hope for observation. The results for Heusler materials or materials with similar electronic structure to bulk HgTe may provide more promising alternatives[53] due to the differences in the sustainable levels of doping.

VI. CONCLUSION

In summary, we performed self-consistent Bogoliubov-de-Gennes calculations to study properties of vortices in doped topological insulators that become superconducting. Through the use of our numerics, we studied the physics of Majorana fermions in vortex lattices beyond the strict weak-coupling limit, and the resulting vortex phase transitions between a topological and trivial state. We have shown that the quasi-particle band spectra offers evidence that there exists an optimal regime in chemical potential where the Majorana fermions can stably reside even in a finite thickness system. There also exists other regimes where the Majorana fermions do not stably exist on the system surfaces because of intra- and inter-surface hybridization between the vortex modes. Furthermore, we also showed that, through the use of the analogous s-wave-TI heterostructure, that TIs with bulk superconductivity containing finite carrier density but insufficient superconducting pairing strength can host Majorana fermions on the surface. Similar to the bulk superconducting case, the Majorana modes can also leak into the bulk and annihilate with the other surface. However, the tunneling behavior exhibits the usual exponential decay with thickness and we conclude that the Majorana fermions can survive for thick samples. Unfortunately, the simple estimates we made for a viable temperature range in which Majorana modes may be observed indicate that superconducting $Cu-Bi_2Se_3$ may not provide a good candidate even if the doping level can be tuned to the topological vortex phase.

ACKNOWLEDGMENTS

[1] P. Hosur, P. Ghaemi, R. S. K. Mong, and A. Vishwanath, Phys. Rev. Lett. **107**, 097001 (2011).

[2] E. Majorana, Niovo Cimento **5**, 171 (1937).

[3] D. A. Ivanov, Phys. Rev. Lett. **86**, 268 (2001).

[4] A. Y. Kitaev, Phys. Usp. **44**, 131 (2001).

[5] F. Wilczek, Nat. Phys. **5**, 614 (2009).

[6] T. L. Hughes, Physics **4**, 67 (2011).

[7] S. Das Sarma, C. Nayak, and S. Tewari, Phys. Rev. B **73**, 220502 (2006).

[8] N. Read and D. Green, Phys. Rev. B **61**, 10267 (2000).

[9] C. Nayak, S. H. Simon, A. Stern, M. Freedman, and S. Das Sarma, Rev. Mod. Phys. **80**, 1083 (2008).

[10] R. Willett, J. P. Eisenstein, H. L. Stormer, D. C. Tsui, A. C. Gossard, and J. H. English, Phys. Rev. Lett. **59**, 1776 (1987).

[11] G. Moore and N. Read, Nucl. Phys. B **360**, 362 (1991).

[12] I. P. Radu, J. B. Miller, C. M. Marcus, M. A. Kastner, L. N. Pfeiffer, and K. W. West, Science **320**, 899 (2008).

[13] A. Y. Kitaev, Ann. Phys. **303**, 2 (2003).

[14] M. Cheng, R. M. Lutchyn, V. Galitski, and S. Das Sarma, Phys. Rev. Lett. **103**, 107001 (2009).

[15] J. Jang, D. G. Ferguson, V. Vakaryuk, R. Budakian, S. B. Chung, P. M. Goldbart, and Y. Maeno, Science **331**, 186 (2011).

[16] L. Fu and C. L. Kane, Phys. Rev. Lett. **100**, 096407 (2008).

[17] J. D. Sau, R. M. Lutchyn, S. Tewari, and S. Das Sarma, Phys. Rev. Lett. **104**, 040502 (2010).

[18] J. Alicea, Phys. Rev. B **81**, 125318 (2010).

[19] R. M. Lutchyn, J. D. Sau, and S. Das Sarma, Phys. Rev. Lett. **105**, 077001 (2010).

[20] Y. Oreg, G. Refael, and F. von Oppen, Phys. Rev. Lett. **105**, 177002 (2010).

[21] V. Mourik, K. Zuo, S. M. Frolov, S. R. Plissard, E. P. A. M. Bakkers, and L. P. Kouwenhoven, Science **336**, 1003 (2012).

[22] C. L. Kane and E. J. Mele, Phys. Rev. Lett. **95** (2005).

[23] C. L. Kane and E. J. Mele, Phys. Rev. Lett. **95**, 146802 (2005).

[24] B. A. Bernevig, T. L. Hughes, and S.-C. Zhang, Science **314**, 1757 (2006).

[25] M. Konig, S. Wiedmann, C. Brune, A. Roth, H. Buhmann, L. W. Molenkamp, X.-L. Qi, and S.-C. Zhang, Science **318**, 766 (2007).

[26] L. Fu, C. L. Kane, and E. J. Mele, Phys. Rev. Lett. **98**, 106803 (2007).

[27] J. E. Moore and L. Balents, Phys. Rev. B **75**, 121306 (2007).

[28] R. Roy, Phys. Rev. B **79**, 195322 (2009).

[29] M. Z. Hasan and C. L. Kane, Rev. Mod. Phys. **82**, 3045 (2010).

[30] D. Hsieh, D. Qian, L. Wray, Y. Xia, Y. S. Hor, R. J. Cava, and M. Z. Hasan, Nature (London) **452**, 970 (2008).

[31] Y. L. Chen, J. G. Analytis, J.-H. Chu, Z. K. Liu, S.-K. Mo, X. L. Qi, H. J. Zhang, D. H. Lu, X. Dai, Z. Fang, S. C. Zhang, I. R. Fisher, Z. Hussain, and Z.-X. Shen, Science **325**, 178 (2009).

[32] D. Hsieh, Y. Xia, D. Qian, L. Wray, J. H. Dil, F. Meier, J. Osterwalder, L. Patthey, J. G. Checkelsky, N. P. Ong, A. V. F. H. Lin, A. Bansil, D. Grauer, Y. S. Hor, R. J. Cava, and M. Z. Hasan, Nature (London) **460**, 1101 (2009).

[33] G. E. Volovik, JETP Lett. **70**, 609 (1999).

[34] C.-K. Chiu, M. J. Gilbert, and T. L. Hughes, Phys. Rev. B **84**, 144507 (2011).

[35] X. L. Qi, T. L. Hughes, and S. C. Zhang, Phys. Rev. B **81**, 134508 (2010).

[36] Y. S. Hor, A. J. Williams, J. G. Checkelsky, P. Roushan, J. Seo, Q. Xu, H. W. Zandbergen, A. Yazdani, N. P. Ong, and R. J. Cava, Phys. Rev. Lett. **104**, 057001 (2010).

[37] Y. Hor, J.G.Checkelsky, D.Qub, N.P.Ong, and R.J.Cava, J. Phys. Chem. Solids. **72**, 572 (2011).

[38] L. A. Wray, S. Xu, Y. Xia, D. Qian, A. V. Fedorov, H. Lin, A. Bansil, L. Fu, Y. S. Hor, R. J. Cava, and M. Z. Hasan, Phys. Rev. B **83**, 224516 (2011).

[39] L. Fu and E. Berg, Phys. Rev. Lett. **105**, 097001 (2010).

[40] H. Zhang, C.-X. Liu, X.-L. Qi, X. Dai, Z. Fang, and S.-C. Zhang, Nat. Phys. **5**, 438 (2009).

[41] C.-X. Liu, X.-L. Qi, H. Zhang, X. Dai, Z. Fang, and S.-C. Zhang, Phys. Rev. B **82**, 045122 (2010).

[42] P. D. Gennes, *Superconductivity of metals and alloys* (W. A. Benjamin Inc., 1966).

[43] O. Vafek, A. Melikyan, M. Franz, and Z. Tešanović, Phys. Rev. B **63**, 134509 (2001).

[44] Y. Wang and A. H. MacDonald, Phys. Rev. B **52**, R3876 (1995).

[45] J. Zak, Phys. Rev. **134**, A1602 (1964).

[46] J. Zak, Phys. Rev. **134**, A1607 (1964).

[47] Q. Han, J. Phys.: Condens. Matter **22**, 035702 (2010).

[48] H.-H. Hung, C.-L. Song, X. Chen, X. Ma, Q.-k. Xue, and C. Wu, Phys. Rev. B **85**, 104510 (2012).

[49] B. Béri and N. R. Cooper, Phys. Rev. Lett. **107**, 145301 (2011).

[50] K. Yasui and T. Kita, Phys. Rev. Lett. **83**, 4168 (1999).

[51] G. E. Shoemake, J. A. Rayne, and R. W. Ure, Phys. Rev. **185**, 1046 (1969).

[52] L. A. Wray, S.-Y. Xu, Y. Xia, Y. S. Hor, D. Qian, A. V. Fedorov, H. Lin, A. Bansil, R. J. Cava, and M. Z. Hasan, Nat. Phys. **6**, 855 (2010).

[53] C.-K. Chiu, P. Ghaemi, and T. L. Hughes, arXiv:1203.2958 (2012).